A highly explicit electrochemical biosensor for catechol detection in real samples based on copper-polypyrrole

Qasar Saleem,[a] Sammia Shahid,[a] Abdur Rahim,*[b] Majed A. Bajaber,[c] Sana Mansoor,[a] Mohsin Javed,[a] Shahid Iqbal, [ID] *[d] Ali Bahadur,*[e] Samar O. Aljazzar,[f] Rami Adel Pashameah,[g] Samah A. AlSubhi,[h] Eman Alzahrani[i] and Abd-ElAziem Farouk[i]

Catechol is a pollutant that can lead to serious health issues. Identification in aquatic environments is difficult. A highly specific, selective, and sensitive electrochemical biosensor based on a copper-polypyrrole composite and a glassy carbon electrode has been created for catechol detection. The novelty of this newly developed biosensor was tested using electrochemical techniques. The charge and mass transfer functions and partially reversible oxidation kinetics of catechol on the redesigned electrode surface were examined using electrochemical impedance spectroscopy and cyclic voltammetry scan rates. Using cyclic voltammetry, chronoamperometry, and differential pulse voltammetry, the characteristics of sensitivity ($8.5699 \ \mu A \ cm^{-2}$), LOD ($1.52 \times 10^{-7} \ \mu M$), LOQ ($3.52 \times 10^{-5} \ \mu M$), linear range ($0.02-2500 \ \mu M$), specificity, interference, and real sample detection were investigated. The morphological, structural, and bonding characteristics were investigated using XRD, Raman, FTIR, and SEM. Using an oxidation–reduction technique, a suitable biosensor material was produced. In the presence of interfering compounds, it was shown that it was selective for catechol, like an enzyme.

1 Introduction

Catechol ($C_6H_6O_2$) and its isomers are used in producing a variety of products. They include colors, anti-aging cosmetics, medication, plastics, insecticides, and photographic materials. The misuse of the material on a massive scale results in the generation of waste material.[1–5] The release of catechol and any of its compounds into the environment presents a risk.[6] Catechol can cause mutations and ruptures in

[a] Department of Chemistry, School of Science, University of Management and Technology, Lahore 54770, Pakistan

[b] Department of Chemistry, COMSATS University, Islamabad, Pakistan. E-mail: abdur.rahim@comsats.edu.pk

[c] Chemistry Department, Faculty of Science, King Khalid University, P. O. Box 9004, Abha 61413, Saudi Arabia

[d] Department of Chemistry, School of Natural Sciences (SNS), National University of Science and Technology (NUST), H-12, Islamabad, 46000, Pakistan. E-mail: shahidgcs10@yahoo.com

[e] Department of Chemistry, College of Science and Technology, Wenzhou-Kean University, Wenzhou 325060, China. E-mail: abahadur@wku.edu.cn

[f] Department of Chemistry, College of Science, Princess Nourah bint Abdulrahman University, P. O. Box 84428, Riyadh 11671, Saudi Arabia

[g] Department of Chemistry, Faculty of Applied Science, Umm Al-Qura University, Makkah 24230, Saudi Arabia

[h] Laboratory Medicine Department, Faculty of Applied Medical Science, Umm Al-Qura University, Makkah, Saudi Arabia

[i] Department of Chemistry, College of Science, Taif University, P. O. Box 11099, Taif 21944, Saudi Arabia

DNA strands.[7] It can cause serious illnesses ranging from rashes on the skin to severe forms of cancer. Although catechol has high pK_a values,[8] $pK_{a1} = 9.25$ and $pK_{a2} = 13.0$, it is found to be un-dissociated under physiological conditions. The introduction of catechol into aquatic systems can originate from natural or artificial sources.[9] Primary sources include the large-scale decomposition of natural material, industrial wastewater, the degradation of lignin in wood pulp,[10] and oil processing units.[11] Because molecular catechol has the propensity to interact with H_2N- and HS-proteins, it is more vulnerable to being absorbed by animals and plants.[12] Under strongly acidic conditions, pure catechol can combine with transition metals like copper and iron to produce complexes.[13]

At an appropriate potential, catechol can go through a reversible redox progression, a two-step oxidation process, that leads to semi-quinone and benzoquinone.[14] Methods like high-performance liquid chromatography,[15] mass spectroscopy,[16] enzymes,[17] chemiluminescence,[18] electrophoresis, and electrochemical methods[19] have all been used to find catechol and its isomers. Every method has pros and cons. To determine an analyte, many parameters could be involved, particularly catechol and its isomers, both of which have similar redox potentials.[20] Detection using nanomaterials, such as transition metals, metal polymers, and conducting polymer composites, has several advantages over all other approaches. The greater density of active sites on the surface of the metal or metal-

conducting polymer composite surface eases the reversibility of catechol oxidation/reduction at the surface.[21] These conducting polymers have excellent chemical and thermal stability, and reproducibility as electrochemical sensor materials. Incorporating metal NP particles in conducting polymers makes the flow of electrons more efficient.[22]

A copper-polypyrrole (Cu-PPy) composite was utilized in this investigation to detect the presence of catechol in real samples and a standard aqueous catechol solution. In the electrochemical oxidation of catechol at pH 7.0–7.4, the composite material (Cu-PPy) is an efficient, stable, and effective catalyst. After testing, the working electrode GCE@Cu-PPy was shown to be an electrochemical biosensor for detecting catechol in real samples. As the isomers of catechol, hydroquinone, and resorcinol have very close oxidation potentials in the range of 200–650 mV, in this work, a broader potential range of −200 to 800 mV was applied for the possible presence of isomeric phenolic compounds. The high specificity of the proposed sensor was observed for catechol, as only a single oxidative peak was recorded in the DPV scan in the range 263.4 to 273.1 mV. This shows the enzyme-like (tyrosinase a copper-based protein) specificity of the material for catechol. As tyrosinase is a copper-containing protein, its parts (H389, H390, h363, h367, H180, H202, H211) which interact with Cu-a and Cu-b ions resemble pyrrole in terms of structure.[40] Interaction between copper NPs and polypyrrole is also evident in Raman and FTIR spectra. In this work, a GCE@Cu-PPy-modified electrode was used to make an electrochemical biosensor that can detect catechol. The Cu-PPy composite was fabricated by a simple redox reaction in an ethanolic environment. Earlier, this composite was reported by Aravindan *et al.* and that research group synthesized this composite by electrochemical deposition.[41] Whereas, in this study a simple chemical oxidation and reduction process was used to synthesize Cu-PPy. Better results in this study make this work distinctive. SEM, XRD, FTIR, and Raman spectroscopy were all used to confirm the material produced. The

electrochemical performance was evaluated for catechol detection, which was carried out by differential pulse voltammetry (DPV). The detection process was optimized by evaluating the effect of pH and scan rate. It is possible to assert that GCE@Cu-PPy is an electrochemical biosensor for catechol detection that is exclusive to catechol detection. The obtained data from CV, DPV, EIS, and chronoamperometry were utilized to create regression graphs.
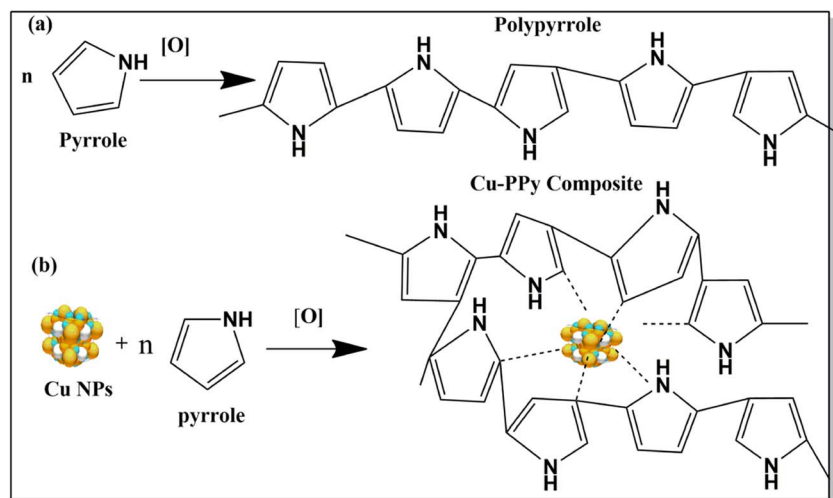
2 Experimental

2.1 Reagents and chemicals

This investigation prioritized the utilization of pure substances of analytical grade. Every chemical was utilized in its purchased form. The purity percentages of all compounds across the board fell between 98 and 99.99%. Copper nitrate (Sigma-Aldrich; 98.5%), sodium borotetrahydride (Sigma-Aldrich; 99.99%), polyvinylpyrrolidone (PVP 40) (Merk), pyrrole (Sigma-Aldrich; 98%), ammonium persulfate (Sigma-Aldrich), hydrochloric acid (Sigma-Aldrich), and Nafion 117 ($C_7HF_{13}O_5S \cdot C_2F_4$; 5% Merck).

2.2 Synthesis of Cu NPs, PPy, and Cu-PPy nanoparticles

Chemical reduction produces copper nanoparticles with appropriate modifications in the reported process.[23] First, 25 mL of 0.0315 M solution of Cu^{2+} (aq) were mixed with polyvinylpyrrolidone (PVP 40) as a capping agent (1 : 6) in a 250 mL beaker and sonicated for 1 hour in an ice-chilled bath. Copper ions were reduced by pouring sodium borotetrahydride (SBH; 0.264 M) dropwise in the presence of PVP 40. After adding 50 mL of SBH at a rate of 0.05 mL/10 s from a burette, the dark brown particles that formed were separated after centrifugation (4000 rpm) for 2 hours. After filtration and washing with distilled water and acetone, particles were dried for 24 hours at 60 °C in an oven and annealed for 6 hours at 550 °C in a muffle furnace. Polypyrrole (PPy) and copper-polypyrrole (Cu-PPy) were

Scheme 1 (a) Formation of polypyrrole (PPy) in the presence of an oxidizing agent (ammonium persulfate). (b) Formation of polypyrrole incorporated around Cu NPs dispersed in pyrrole. Dotted lines show the interaction between π electrons, N−H, and copper NPs.

simultaneously produced through chemical oxidation in ice-chilled baths. After setting up an ice bath, a 100 mL mixture of double deionized water (DDIW) and absolute ethanol (1 : 1) was added; then 10 mL of HCl (37%) and 1 mL of pyrrole (98%) were added in 250 mL beakers. After 1 hour of sonication, 0.01 mg of Cu NPs were transferred to one beaker and subsequently sonicated for an additional 30 minutes. Then, 50 mL of 0.02 M ammonium persulfate were simultaneously poured into both beakers containing pyrrole and Cu NPs-pyrrole. After 24 hours, the blue-black particles were spun in a centrifuge (4000 rpm), and the particles that settled to the bottom were separated from the solvent by careful decanting. The composite obtained was washed rigorously with DDIW and acetone followed by drying of the produced particles for 36 hours in an oven at 60 °C. The reported approach was successfully modified[24] to finish this synthesis process, as shown in Scheme 1.

2.3 Material characterization

Structural analysis was undertaken using a monochromatic Cu-K radiation (1.5418 nm) source on a PANalytical powder X-ray diffractometer. The crystallite sizes of Cu NPs, PPy, and Cu-PPy were computed with Scherrer's equation ($D = \kappa\lambda/\beta\cos\theta$), where D is the average size of the crystalline domains, κ is the shape factor (0.9), β is the full-width at half maximum, θ is the Bragg angle, and λ is the X-ray wavelength in nanometers (0.15418 nm). The surface morphologies of Cu-PPy, PPy, and Cu NPs were determined using a Zeiss scanning electron microscope operating at 20 kV, with signal A = C2DS. The average particle size was measured with ImageJ software version 1.53. For the elemental analysis of the samples, energy dispersive spectroscopy (EDX) was performed. A Thermo-Nicolet 6700 P FTIR spectrometer (United States) was utilized for a functional group confirmation Fourier transform infrared spectroscopy investigation in the region of 4000 to 600 cm^{-1}. A Gamry potentiostat (Ref. 3000, Model No. 43120) was used for electrochemical studies under ambient laboratory conditions. A three-electrode configuration consisting of a glassy carbon electrode (GCE) modified with Cu NPs, PPy, and Cu-PPy nanostructures as the working electrodes, Ag/AgCl (3 M KCl) as the reference electrode, and platinum wire as the counter electrode was utilized for electrochemical investigation. Cyclic voltammetry (CV), chronoamperometry, differential pulse voltammetry (DPV), and electrochemical impedance spectroscopy (EIS) were utilized to measure electrochemical activity. A Raman shift study was performed using a Renishaw UK InVia Raman microscope. Laser used for excitation: 514 nm laser; 10 s 1800 I/mm grating exposure time. Objective: 100% laser power for ×50LL.

2.4 Fabrication of catechol-sensing modified electrodes

A modified version of a method described in the literature[25] was used to polish four Gamry glassy carbon electrodes (active face area = 0.37714 cm^2). First, 0.1 mg of Cu NPs, PPy, and Cu-PPy were separately added to 10 μL of acetone containing 1 μL of diluted Nafion (5% Nafion in 5 mL of acetone) and sonicated for 10 minutes. Separately, 1 μL of each dispersed slurry was

applied to the active polished faces of three GCEs by drop casting with a micropipette. To ensure equal drying of the coating, the cast faces of three GCEs were placed 8 cm beneath a 60 watt tungsten light bulb (60 °C to 70 °C) for 30 minutes. The modified electrodes were labeled as bare GCE, GCE@Cu, GCE@PPy, and GCE@Cu-PPy. In a 0.1 M phosphate buffer solution (PBS) with 1.0 M KCl as the supporting electrolyte, the electrochemical responses of all modified working electrodes were evaluated in the presence of 100 μL of catechol ([CAT] = 5 mM), with platinum wire serving as the counter electrode (CE) and Ag/AgCl serving as the reference electrode (RE). Fig. 1a shows the cyclic voltammetry (CV) responses of four electrodes with a scan rate of 50 mV s^{-1} and a potential range of −0.15 to 0.7 V (−150 mV to 700 mV). The GCE@Cu-PPy (WE) electrode response was superior (I_{pa} = 83.75 μA, E_{pa} = 583 mV) to all others. GCE@Cu-PPy was used as the biosensor material, and a study of the electrochemical biosensor response for catechol detection was accomplished.

2.5 Real sample preparation

The viability of the proposed sensor was confirmed using a real catechol sample solution. A commercial physiological solution (sodium chloride 0.9% w/v) was purchased from Otsuka, Pakistan Ltd.; and a 5 mM catechol solution was prepared in a physiological solvent. A catechol solution with a known concentration (5 mM) was injected into an electrochemical cell. A separate plot with a higher oxidative current peak accompanied each addition. A set of amperograms were measured in the range 100–1000 μL (stock 5 mM) range.

2.6 Effect of pH

The pH of the electrolyte has a significant effect on the oxidation peak current and peak potential of the analyte during oxidation. The anodic peak potential of CAT, as shown in Fig. 1c was found when the pH rose from 1 to 13, and a positive shift occurred. The value of the slope of the line-plotted pH levels and peak potentials, as illustrated in Fig. 1d, shows that the linearity is good. The value of the slope for CAT is 0.02799 V pH^{-1}, indicating that the number of electrons and protons is equal to the process of oxidation. The maximum anodic current of CAT oxidation in the pH range of 7.0–7.4 expands as the concentration of acidic substances rises. Secondly, a decrease in the current peak was seen between pH 8 and 13 (basic pH). At pH 7.0–7.4, the electrode passed full current. According to this outcome, it is clear that the oxidation potential and anodic peak current for CAT are significantly affected by the pH. For construction we chose the most efficient sensor for biological samples. pH 7.0–7.4 and potential range −0.15 to 0.7 V were chosen for further electrochemical studies. As shown in Fig. 1c and 7c the effect of pH was not linear; the maximum current response was recorded between pH 7.0 and 7.4, but decreased as the pH increased beyond 7.4.

2.7 Effect of scan rate

To estimate the electron-transfer kinetics of CAT oxidation at GCE@Cu-PPy, the effect of the scan rate was investigated.
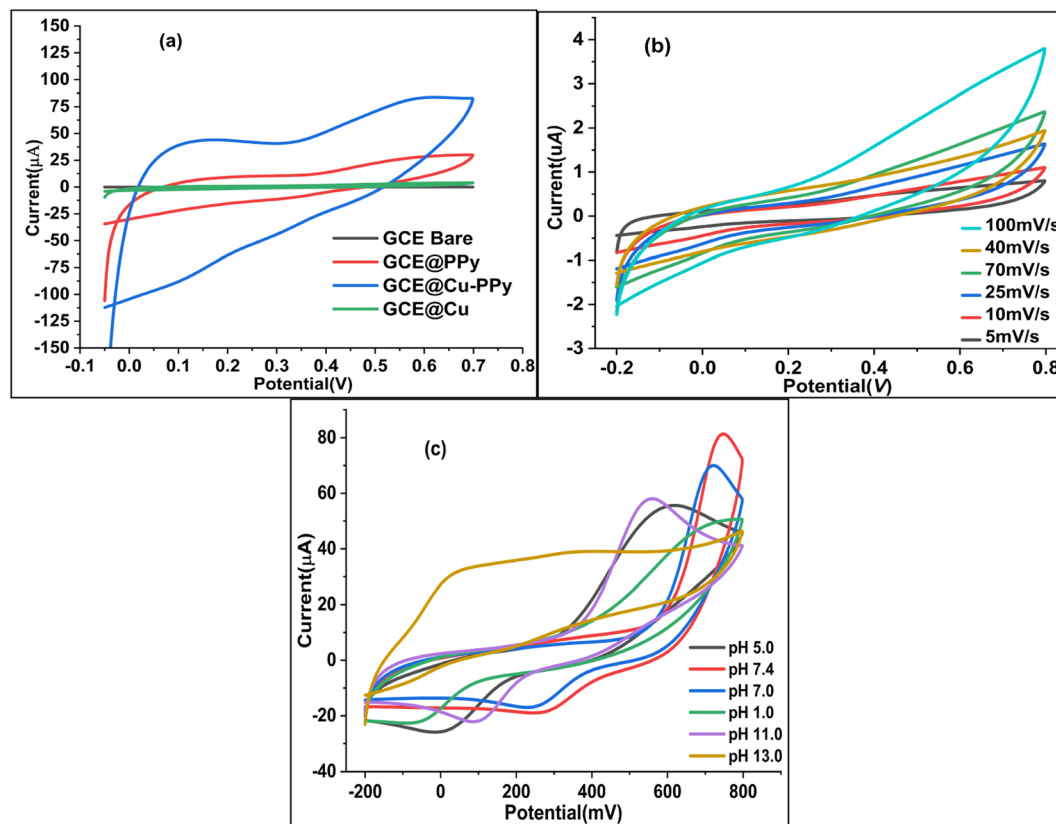
Fig. 1 Electrochemical responses of bare GCE and modified electrodes in 0.1 M PBS/1.0 M KCl: (a) comparative voltammograms of bare GCE, GCE@Cu, GCE@PPy, and GCE@Cu-PPy; (b) scan rate voltammograms from 5 mV s^{-1} to 100 mV s^{-1}; (c) pH study showing CV plots at various pH values (pH 5 to 13) against current (μA).

Fig. 1b shows the cyclic voltammogram data of 100 μL of CAT acquired in 0.1 M PBS/1 M KCl at various scan rates ranging from 5 mV s^{-1} to 100 mV s^{-1}. Fig. 1b shows that the I_{pa} value increases as the scan rate increases, while the E_{pa} value increases on the positive side. This trend is likely because the kinetic energy of the reaction between the CAT molecules and the active sites of the GCE@Cu-PPy electrode are restricted. This is in agreement with the research that has been conducted. As shown in Fig. 1b, the fact that the I_{pa} value of CAT oxidation varies linearly in response to variation in the scan rate is proof that the electrode process is surface-controlled. Despite this, the plot of I_{pa} *versus* the square root of scan rate ($\nu^{1/2}$) (Fig. 7b) was linear, with the linearity most likely attributable to the diffusion-controlled CAT oxidation process.

Eqn (1) and (2) describe the anodic portion of the oxidation reaction. Depending on scan rates, it can be concluded that the electrochemical oxidation of CAT involves a combination of diffusion and adsorption-regulated mechanisms. Therefore, the oxidation process of catechol at the surface of GCE@Cu-PPy was quasi-reversible.

$$I_{pa} \ (\mu A) = 5.049747\nu^{1/2} \ (mV^{1/2} \ s^{-1/2}) + 5.6541 \ (\mu A) \quad (1)$$

$$I_{pc} \ (\mu A) = -2.1577\nu^{1/2} \ (mV^{1/2} \ s^{-1/2}) - 0.80928 \ (\mu A) \quad (2)$$

($R^2 = 0.97858$), where ν (mV s^{-1}) represents the scan rate.

2.8 Optimization of electrochemical investigation conditions

As pH and scan rate studies with GCE@Cu-PPy against the reference electrode Ag/AgCl have proven that the oxidation of catechol at the surface of the working electrode is a diffusion phenomenon and is pH dependent, a further study was carried out at pH 7.0–7.4 at a scan rate of 50 mV s^{-1}. Regression plots, as shown in Fig. 7b, I_{pa} *vs.* $\nu^{1/2}$ and I_{pc} *vs.* $\nu^{1/2}$, show that the redox process at the surface of the electrode is diffusion-based.[29] The kinetics of the reaction are equal to one proton against one electron.[30] Whereas Fig. 7c shows the change in redox current against variable pH, the data suggested a pH of 7.0–7.4 for further studies to detect catechol. The correlation equations, eqn (1) and (2), are derived from the regression plots.

3 Results and discussion

3.1 X-ray diffraction (XRD) analysis

The phase and crystallinity of the synthesized particles were determined based on the XRD results. The significant peak positions of Cu-PPy are as follows: 24.138°, 33.153°, 35.612°, 39.277°, 40.855°, 43.519°, 49.480°, 54.091°, 56.152°, 57.429°, 57.590°, 62.451°, 62.744°, with corresponding index values of (0 1 2), (1 0 4), (1 1 0), (0 0 6), (1 1 3), (2 0 2), (0 2 4), (1 1 6), (2 1 1), (1 1 2), (0 1 8), (2 1 4), (3 0 0), (2 2 0). Data were used to calculate the
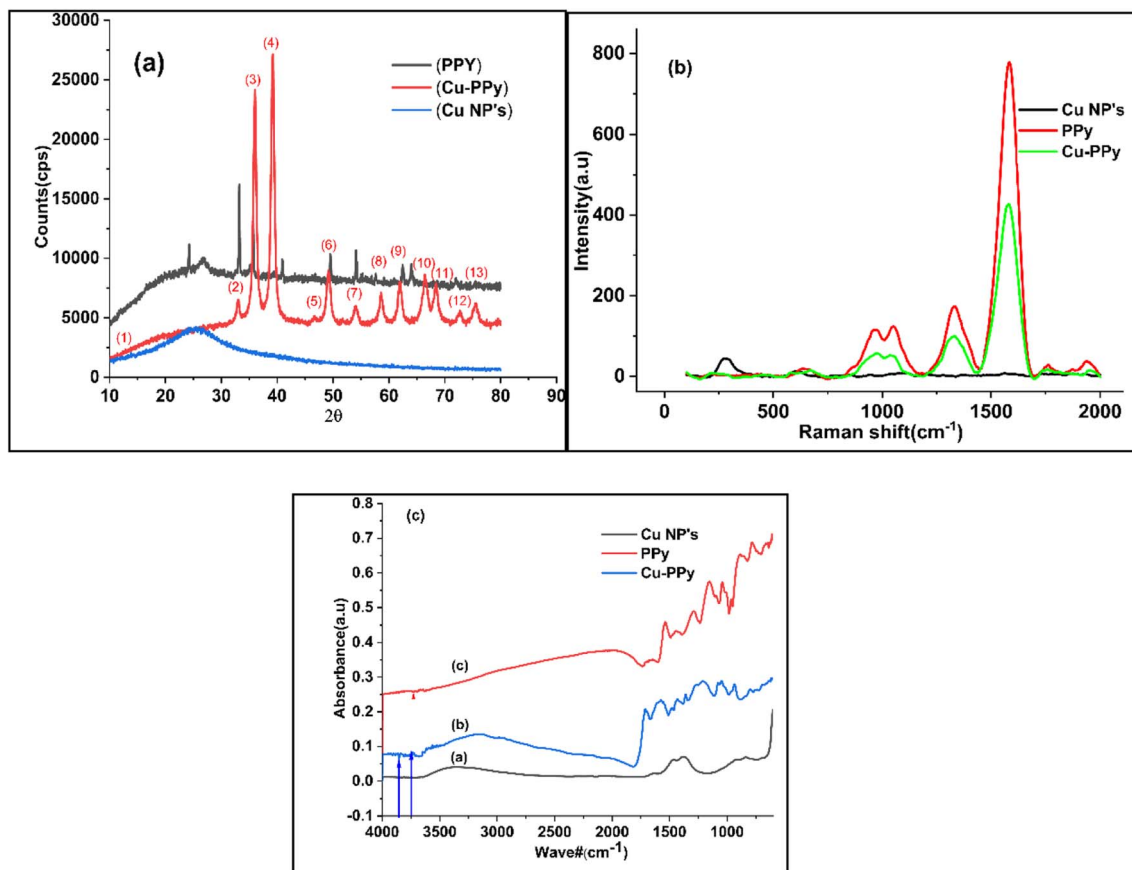
Fig. 2 Data plots of Cu NPs, PPy, and Cu-PPy: (a) XRD spectra of Cu NPs, PPy, and Cu-PPy; (b) Raman shift spectra of Cu NPs, PPy, and Cu-PPy; (c) FTIR absorbance spectra of (a) Cu NPs, (b) PPy, and (c) Cu-PPy.

crystallinity and strain % of Cu NPs, PPy, and Cu-PPy,[26,27] which computed crystallite sizes of 510, 349.5, 106.3636 Å and strain percentages of 0.495857%, 0.3348%, and 0.495857%, respectively. The database matched the JCPDS cards 96-222-4614 and 96-222-4614, space group $R\bar{3}c$, and space group number 167. As can be seen in Fig. 2a, the position of the intense peak at $2\theta = 33.15$ in the PPy plot migrated to 35.87 in the Cu-PPy composite plot. The same pattern (right shift) was observed for the remaining peaks. As expected, the Cu NPs were disseminated within the polymer and interacted with the polar ends (–NH) or π electrons of the polymer chain.[28] The pattern of peaks in PPy and Cu-PPy indicated that a composite material was successfully formed. Cu NPs, PPy, and the Cu-PPy composite had average particle sizes of 179 nm, 286 nm, and 402 nm, with standard deviations of 16.35533, 17.09714, and 17.09714, respectively. By comparing the peaks with JCPDS cards (00-035-0816, 01-073-1667), the anorthic shape of Cu NPs and the rhombohedral nature of PPy and Cu-PPy were confirmed. Scherrer's formula, $D = \kappa\lambda/\beta\cos\theta$, was used to calculate the crystallite sizes.[30] Fig. 2a reveals a 2.3° right shift in the peaks of Cu-PPy compared to neat PPy, which shows that the polar ends (C=N–H, or C=C) of PPy were incorporated with the copper NP particles and enabled smooth charge transfer at lower resistance (R_{ct}) at the electrode surface.

Scanning electron microscopy (SEM) analysis provides information about surface morphology. The nanostructures of Cu NPs, PPy, and Cu-PPy comprise anorthic and rhombohedral shapes, as shown in Fig. 3a–c. The phases and crystallinity of the substance are distinctively anorthic and rhombohedral, respectively, as per the XRD results, evaluated and simulated by X'pert HighScore Plus and matching the peak data with JCPDS cards. Using ImageJ 153 software, the SEM results were evaluated to determine the sizes of the synthesized particles. The average particle sizes were found to be 179 nm, 286 nm, and 402 nm, respectively, as shown in Fig. 3a–c which are in agreement with the results calculated by the Scherrer calculator tool of X'pert HighScore Plus software.

3.2 EDX analysis

EDX analysis provides information about a composite's elemental composition. Fig. 3a–c illustrate the EDX spectra of Cu NPs, PPy, and Cu-PPy, respectively. The existence of Cu, N, C, and O indicates that the intended composite has formed. The values of cps/eV at 1.35 and 88.1 eV (Fig. 3d) suggest that Cu NPs were successfully embedded in polypyrrole. SEM analysis was performed on the used composite particles after testing; no morphological changes were found, as shown in Fig. 8b. The elemental composition of the composite is presented in Table 1.
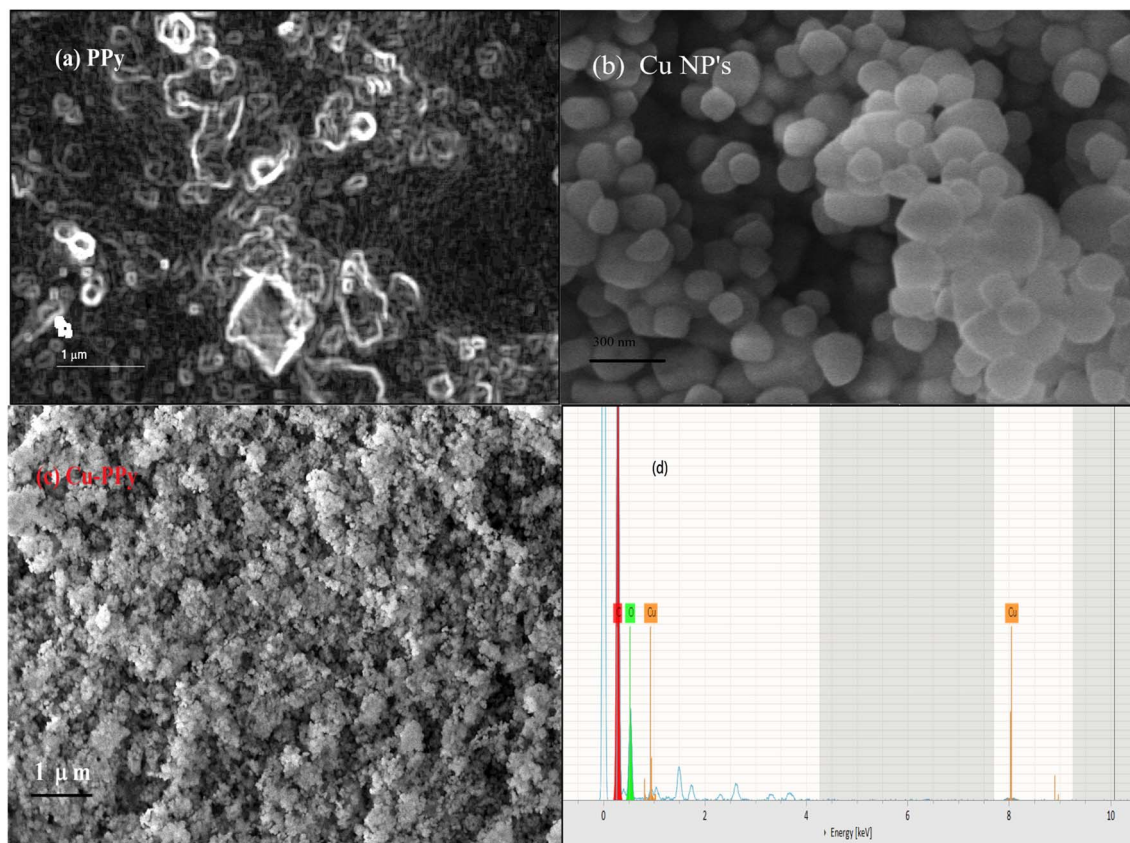
Fig. 3 Surface morphology of PPy, Cu NPs, and Cu-PPy; SEM micrographs: (a) PPy, (b) Cu NPs, (c) Cu-PPy composite. (d) EDX: energy dispersive spectra of Cu NPs.
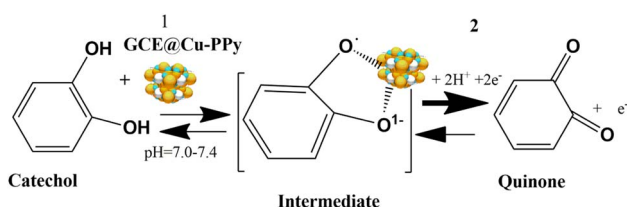
Table 1 EDX elemental composition in the Cu-PPy composite

Element	Atomic no.	Mass (%)	Atomic (%)
Carbon	6	61.86	68.21
Oxygen	8	27.47	22.74
Copper	29	1.47	0.35
Nitrogen	7	9.20	8.70

3.3 Raman shift analysis

Utilizing Raman spectroscopy, the structural compositions of the new Cu NPs, PPy, and Cu-PPy nanocomposite were further investigated. The Raman spectra of Cu NPs, PPy, and Cu-PPy are depicted in Fig. 2b. For Cu-PPy, characteristic peaks consistent with the symmetric stretching of monomers present in the

Scheme 2 Oxidation of catechol at the surface of GCE@Cu-PPy.

polymers appeared at 637, 966, 1050.74 cm^{-1}, with a small shift (12 cm^{-1}) from PPy, most likely as a result of the interaction (as shown in Scheme 2) between Cu NPs and PPy electron-enriched centers (C=NH, or C=C) that is also evident in the XRD data. The Raman spectrum of pure PPy has well-defined peaks at 630, 961, 1055, and 1336 cm^{-1}. The peak in Fig. 2b at 219 cm^{-1} can be correlated to the Raman active mode of moving copper cations along the crystallographic X-axis, whereas the peaks at 281 and 390 cm^{-1} mark the Raman active E_g mode, and that at 600 cm^{-1} may originate from the symmetric breathing mode of O atoms associated with individual Cu cations in the plane perpendicular to the X-axis. Peaks at 1396 and 963 cm^{-1} were caused by the second harmonic vibrational mode. No peaks originated from the PPy polymer; however, typical carbon bands D and G were observed at 1333 and 1586 cm^{-1}, respectively. While a decrease in the peak intensity of PPy defines the development of a new composite with the incorporation of Cu-doped PPy polymer (Cu-PPy). Also, the results of the Raman analysis match those of the XRD analysis, which shows that the nanocomposite used for targeting has grown.

3.4 Fourier transform infrared spectroscopy (FTIR) analysis

FTIR spectra were obtained to confirm that PPy and the Cu-PPy nanocomposite exhibit distinct interatomic bonding. The FTIR spectra in Fig. 2c revealed a unique band at 568 cm^{-1} that can

be attributed to the vibration in the anorthic and rhombohedral sites of Cu NPs, PPy, and Cu-PPy, providing additional evidence for the creation of Cu-PPy that is consistent with XRD and Raman data.

3.5 The electrochemical response of GCE@Cu-PPy

As depicted in Fig. 1a, the GCE@Cu-PPy sensor was more advantageous; hence, GCE@Cu-PPy was utilized in the following electrochemical study. Considering the influence of pH, CV scans were performed in the presence of 100 μL CAT in 0.1 M PBS/1 M KCl, with solution pH ranging from 5.0 to 13. As depicted in Fig. 1c, I_{pa} increased and E_{pa} moved to the right. At pH 13, there are two oxidative peaks at 0.03 V and 0.34 V, which may lead to the dissociation of water molecules. At pH 7.4, the I_{pa} value was extraordinarily high, but the E_{pa} value shifted to the right; this could also result in water splitting. I_{pa} vs. pH and E_{pa} vs. pH regression curves were constructed to optimize pH for further electrochemical study ($R^2 = 0.9875$).

The LOD, LOQ, linearity, and sensitivity of the GCE@Cu-PPy electrode as an electrochemical biosensor for catechol were determined by measuring CV responses over a broad range of blanks and a varying amount of catechol (CAT) in the presence of 0.1 M PBS/0.1 MKCl at a scan rate of 50 m V s^{-1}. By using eqn (3) and S/N (signal to noise ratio), LOD, LOQ, and sensitivity were calculated as: 1.52×10^{-7} μM, 3.52×10^{-5} μM, and 8.5699 μA cm^{-2}, respectively.

The correlation equation was derived as:

$$I_{pa} (\mu A) = 1 \times 10^{-8} [CAT] (\mu A \, \mu M^{-1}) + 2.5707 (\mu A) \quad (3)$$
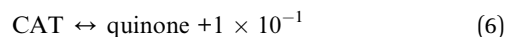
where [CAT] represents the concentration of catechol (stock; 5 mM) solution injected.

$$E = E° + [(RTk_s/nF) + \ln(\nu)] \quad (4)$$

$$E_{pa} = 0.01808 \ln \nu + 0.54011 \quad (5)$$

By using the Laviron equations, eqn (4) and (5), a value of $n = 1$ was calculated, as the reaction is dependent on diffusion.[32]

Here n is the number of electrons involved in the redox process at the surface, $E° =$ standard potential, $k_s =$ rate constant, $T = 298$ K, $F = 96\,500$ cm^{-1}, $R =$ gas constant, $\sigma =$ diffusion factor, and $E =$ reaction potential.[31]

$$CAT \leftrightarrow \text{quinone} + 1 \times 10^{-1} \quad (6)$$

Diffusion and reaction kinetics were also determined by the electrochemical impedance (EIS) technique, to validate the method. Initially, four modified electrodes were tested, as shown in Fig. 5a. In 25 mL of 0.1 M PBS/1.0 M KCl and 5 mL of 5 mM ferro/ferri solution, bare GCE, GCE@Cu, GCE@PPy, and GCE@Cu-PPy were scanned in the presence of 100 μL of CAT solution. The GCE@Cu-PPy results were far better than those for the rest of the electrodes. GCE@Cu-PPy lowers the real (Z_{real}) and imaginary (Z_{img}) impedance many-fold compared to the other electrodes demonstrated in Fig. 5a.[32]

In Fig. 5b, the EIS results also support the claim of charge transfer and diffusion at the electrode surface. The resistance to charge transfer (R_{ct}) increases, and the radius of the circular part of the plot representing transfer resistance also increases, as the concentration of analyte CAT increases.

The uniform increase in R_{ct} and the diffusion factor corresponding to the increase in analyte confirm the diffusion phenomena at the surface of the working electrode. The EIS was used to determine the charge transfer and diffusion processes, where the angular frequency indicates the charge transfer and the 45°-inclined line represents the Warburg diffusion factor (σ). The data in Fig. 5a was acquired by employing EIS so that 200 μL of 1.0 M KCl was mixed into 25 mL of PBS and a fixed AC potential of 5 mV and a DC potential of 0.5 V were set at a frequency range of 0.1 to 100 000 Hz. The results over a wide range (100–1300 μL) of [CAT] were promising, as a modest change in charge transfer (R_{ct}) was detected, although the diffusion factor remained constant at 45° against an equal induction of [CAT]. The overall changes in Z_{real} were 1.011, 405 (84, 72, 348 Ω μL^{-1}). With the acquired plots, an equivalent circuit (CPE with diffusion) was precisely matched (inset). With increasing [CAT], the charge transfer resistance (R_{ct}) increased
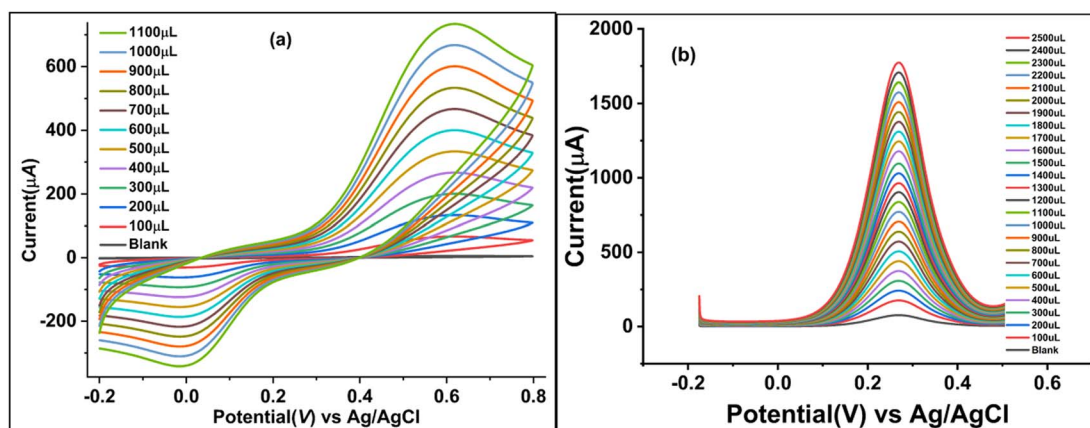

Fig. 4 Electrochemical responses of GCE@Cu-PPy as a CAT sensor: (a) CV voltammograms of GCE@Cu-PPy at different concentrations of CAT (100–1100 μL), (b) DPV plots at different concentrations of CAT (100–2500 μL).
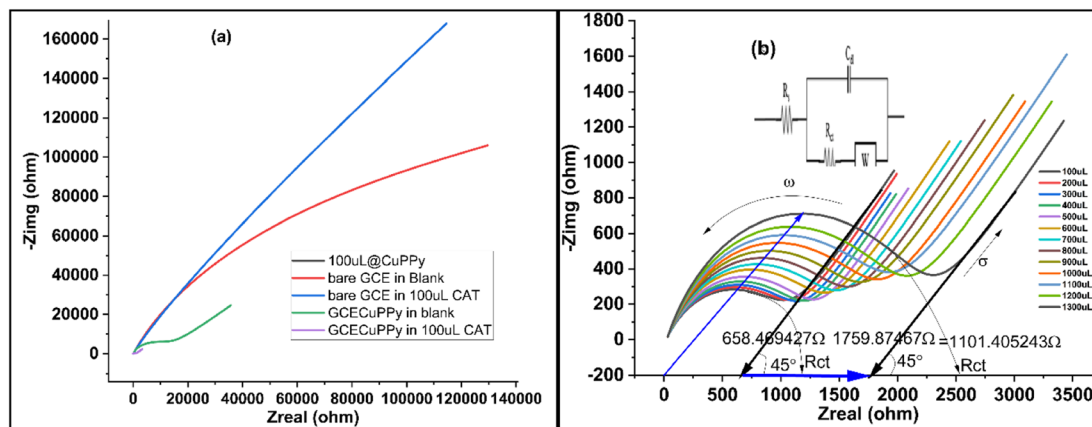
Fig. 5 (a) EIS (Nyquist plot) comparison of CAT with bare GCE and modified GCE@Cu-PPY working electrode in the blank solution and in the presence of 100 μL of CAT. (b) Nyquist plots with varying [CAT], GCE@Cu-PPy as working electrode at different concentrations of CAT (100–1300 μL); inset: equivalent circuit (CPE; constant phase element with diffusion).

steadily ($2.215 \times 10^3 \ \Omega$). The diffusion factor (σ) was constant for equal additions of [CAT]. The EIS results are shown in Fig. 5b.

3.6 Electrochemical biosensor performance of GCE@Cu-PPy

Due to the favorable electrochemical response of the synthesized catalyst/biosensor GCE@Cu-PPy, it was assessed as an enzyme-free biosensor for catechol detection. The CV responses were measured for a broad range of CAT concentrations (100–1100 μL) in 25 mL of 0.1 M PBS containing 1.0 M KCl as a supporting electrolyte, as shown in Fig. 4a. To identify trace impurities in the CAT standard solution, as depicted in Fig. 4a, a broad potential window (−0.2 to 0.8 V, at a scan rate of 50 mV⁻¹) was set up. 0.615 V against 1100 μL [CAT] produced the greatest rise in I_{pa} (738.45 μA). The suggested biosensor is linear over a wide concentration range. High catalytic effects and smooth conductivity were observed in the synthesized sensor, which remained stable and effective. Oxidative peak potential moved to the right by only 0.016 mV, but the reductive peak

potential shifted to the left. The increase in I_{pa} (738.45 μA) was more than the change in I_{pc} (−342.62 μA), which shows that partial oxidation at the electrode surface could be reversed.

3.7 Differential pulse voltammetry (DPV) response of GCE@Cu-PPy

The DPV method is more sensitive than the cyclic voltammetry (CV) method, as shown in Fig. 4b, and the DPV technique was used to scan a wide range of catechol concentrations, from 100 μL to 2500 μL, in batches that consistently increased in concentration. In all of the different concentrations of catechol, I_{pa} peaks at an almost fixed E_{pa} (261–270 mV) were observed. At a potential of 270 mV, the rise against a 2500 μL CAT injection was noted to be at its greatest. A broad potential window spanning −0.2 to 0.7 V was chosen to identify any other potentially disruptive species. A sharp peak that is persistent in the range 261–270 mV indicates the specificity of the proposed stable catalyst/sensor for catechol as no other peak was observed.
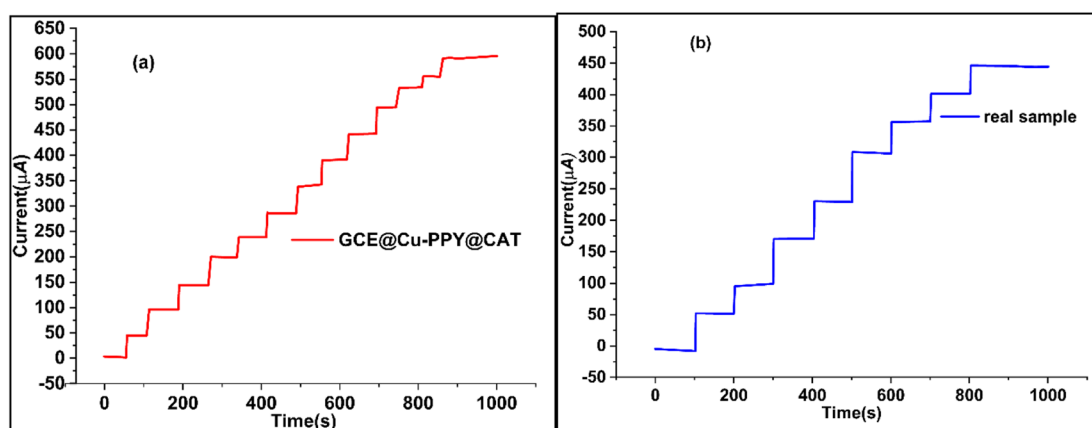

Fig. 6 (a) Chronoamperometry plot of a standard solution of CAT (5 mM) with injection at 100 μL/50 s, (b) chronoamperometry of CAT in a real sample with injection at 100 μL/100 s.

Table 2 Comparison of LOD, linear range, and sensitivity of the materials with the literature

Sr. No.	Sensor	Linear range	The detection limit (LOD)	Sensitivity	Reference
1	COF	4.0 to 450 450 µM	0.36 µM		33
2	Co-AlMWCNTs	0.5–150 µM	0.074 µM		34
3	Nano-flake graphite	1–100 µM	0.2 µM		35
4	PANI/HSr$_2$Nb$_3$O$_{10}$/GCE	0.025–4.97 mM	0.02 µM		36
5	FePP	50.0–1600.0 µM	0.09 µM		37
6	PtNiCu@FTO	−3000 µM	0.29 µM	1485 µA mM^{-1} cm^{-2}	38
7	Nitrogen-doped hollow carbon spheres	0.5 and 300 µM	0.14 µM		39
8	Cu-PPy/GCE	0.05–1000 µM	0.010 µM		41
8	GCE@Cu-PPy	0.02–2500 µM	1.52×10^{-7} µM	8.5699 µA µM cm^{-2}	This work

3.8 Chronoamperometry response of GCE@Cu-PPy

Chronoamperometry was utilized to determine the sensitivity, selectivity, specificity, and stability of the proposed sensor (GCE@Cu-PPy) for catechol detection in a real sample. The working electrode GCE@Cu-PPy was used to record chronoamperometry responses against a wide range of catechol concentrations (0 to 2000 µL), as shown in Fig. 6a. The maximum allowable potential was set at 0.5 V. The initial 50 seconds of the current sweep were performed in a solution containing no analyte (blank) (1.0 M KCl/0.1 M PBS). Every 50 seconds up to 1000 seconds, 100 µL of catechol was injected

with a micropipette. A steady increase in current was detected with each 100 µL CAT injection. An increase in current proportional to catechol concentration demonstrates that GCE@Cu-PPy is an efficient, stable, and sensitive enzyme-free CAT biosensor. The average current increased by 55.5248 µA against every addition of 100 µL of CAT.

3.9 Chronoamperometry study of GCE@Cu-PPy: real water sample

To demonstrate the efficacy of the GCE@Cu-PPy catalyst as an enzyme-free biosensor for CAT detection, chronoamperometry
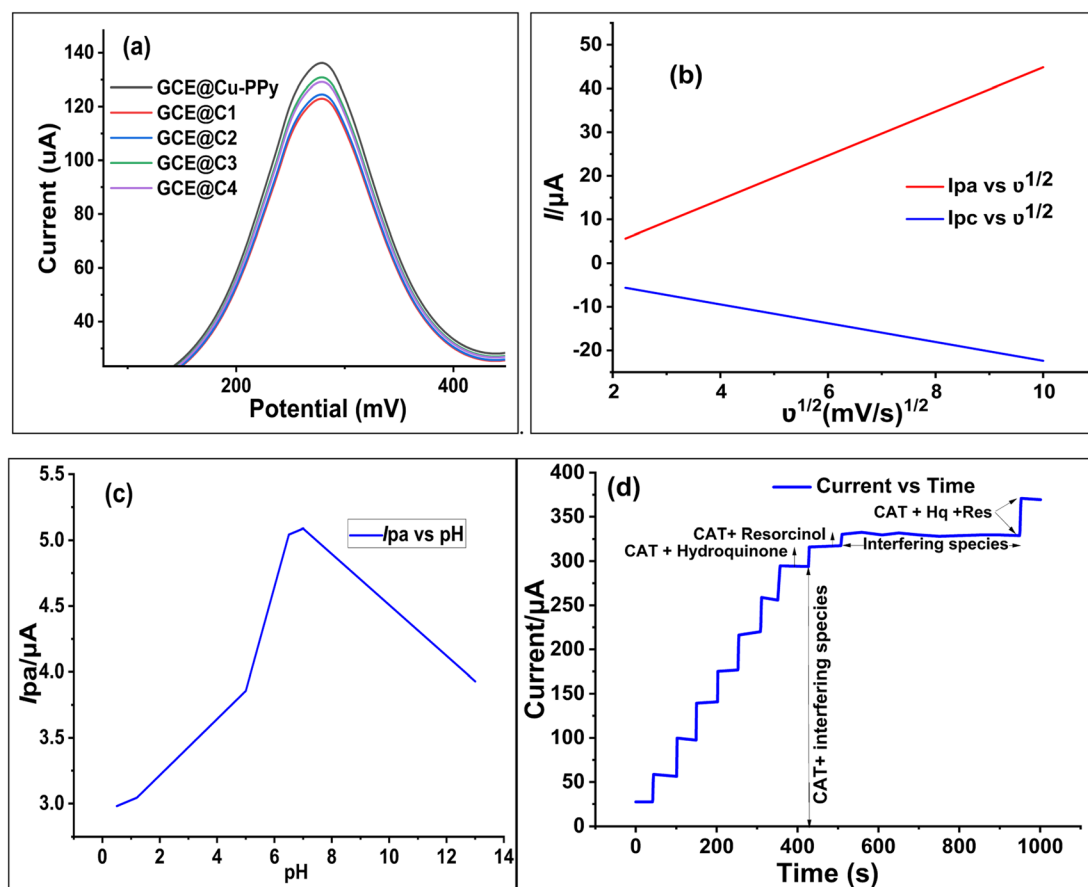

Fig. 7 (a) DPV plots after four weeks in the presence of 500 µL (5 mM) of CAT with four electrodes stored at room temperature. (b) Oxidative current (I_{pa}) *vs.* square root of scan rate ($\nu^{1/2}$) and reduction current (I_{pc}) *vs.* square root of scan rate ($\nu^{1/2}$) plots. (c) I_{pa} *vs.* pH. (d) Amperogram interference study with GCE@Cu-PPy biosensor in the presence of interfering species injected at a rate of 100 µL/100 s CAT solution.

was performed on a real water sample under the same conditions as described above. For the catechol standard solution (5 mM) represented in Fig. 6b, the identical technique was followed. The analyte injection rate was 100 μL/100 s. As described in the section on reagents and chemicals, a real sample was prepared by dissolving catechol in a physiological water sample (0.9% NaCl) acquired from a pharmaceutical source. It was injected at 100 μL per 100 seconds into 25 mL of buffer (0.1 M PBS/1.0 M KCl) solution. The recorded responses are depicted in Fig. 6b. The results were linear and practical, proving the use of the catalyst as a biosensor for catechol. A current increase of 55.83425 μA was recorded, which is the same as that of a standard solution of catechol in DDIDW (Fig. 6a). R^2 in this instance was 0.9995. The performance of GCE@Cu-PPy was compared with similar work from the literature, as presented in Table 2.

From the data in Table 2 it is evident that the synthesized material Cu-PPy is more efficient and specific for the detection of catechol compared to the competing work of Arsalan et al.,[38] as mentioned in Table 2.

3.10 Specificity of catalyst: interference/instantaneous behavior of biosensor GCE@Cu-PPy

To assess the influence of interfering species, a somewhat different strategy was employed. The analyte CAT (5 mM) and 50 mM interfering species solutions were prepared using physiological water acquired from a medical supply company. The analyte (CAT) solutions were prepared with the same concentration that was formerly utilized for CV analysis and chronoamperometry in the presence of interfering species. As interference species, selected resorcinol (R_{es}), hydroquinone (H_q), glucose, 2-nitrophenol, ascorbic acid, benzoic acid, gallic acid, 4-amino phenol, 8-hydroquinone, dopamine, ascorbic acid, K^+, Na^+, Cl^-, SO_4^{2-}, NO_3^-, Mg^{2+}, CO_3^{2-}, I^-, and Br^-. The solutions of catechol, (catechol + resorcinol), (catechol + hydroquinone), and interfering species were injected separately in identical quantities, whereas the solution containing the interfering species was produced by dissolving all of the aforementioned chemicals in proportional amounts. The scanning

technique (chronoamperometry) was performed for the actual sample, and the analyte addition sequence is displayed in Fig. 7d. There was little suppression in oxidative current when hydroquinone and resorcinol were injected along with CAT after 450 s. Whereas, when a solution of interfering species alone was injected, only a wavy line was recorded from 550 s to 950 s. A similar rise in current was recorded when a mixture of all isomers of catechol (catechol + hydroquinone + resorcinol) was injected.

Based on correlation graphs, all the chronoamperometry scans indicated linearity. The repeatability and specificity of GCE@Cu-PPy were examined utilizing DPV (Fig. 4b), which was scanned between 100 μL and 2500 μL of [CAT]. The results revealed a consistent increase in I_{pa} at a single E_{pa} value of 0.270 V; the regression plot of I_{pa} versus [CAT] demonstrated the highest level of confidence; $R^2 = 9997$. As isomers of catechol, resorcinol, and hydroquinone have similar redox potentials; however, the DPV and CV scans did not reveal any additional peaks of I_{pa}/I_{pc}.

3.11 Determination of the stability and reproducibility of the proposed sensor

To determine the reproducibility and storage stability of the GCE@Cu-PPy sensor, four similar GCEs were modified with Cu-PPy slurry from the same source. Electrodes were labeled with the designations GCE@C1, GCE@C2, GCE@C3, and GCE@C4. The electrodes were dried for ten minutes at 60 °C Celsius in an oven. The dried electrodes were stored for four weeks in an airtight plastic container at room temperature. On the 31st day, a DPV scan was conducted through 0.1 M PBS/1.0 M KCl in the presence of 500 μL (5 mM) of CAT solution. The procedure was repeated under the same working potential and concentration settings. All electrode responses were recorded as shown in Fig. 7a, and regression data were obtained, at a recovery rate of 93.68% of the prepared electrodes. All the stored electrodes exhibited a high degree of stability, while the standard deviation of the data was 6.33%, a difference from the original. GCE@Cu-PPy from four electrodes indicated a better degree of
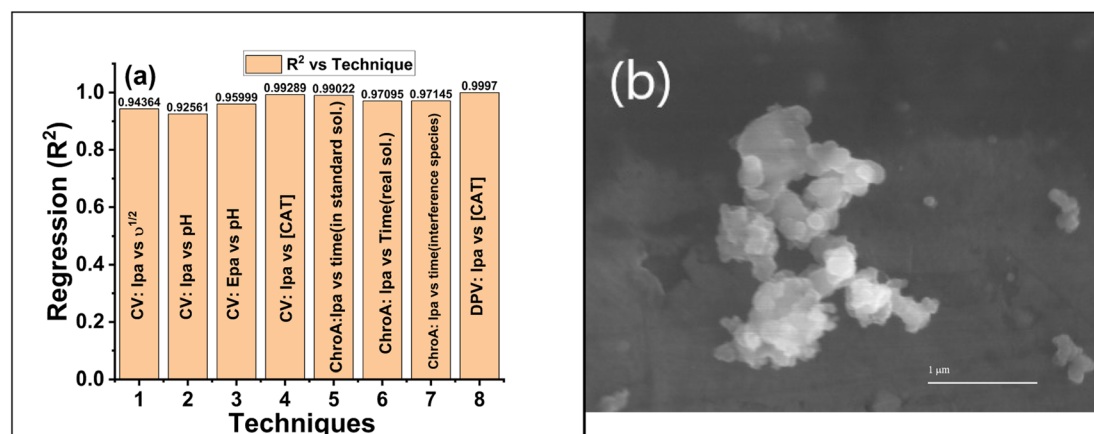

Fig. 8 (a) Comparison regression (R^2) vs. techniques used in the electrochemical study of GCE@Cu-PPy. (b) SEM image of the Cu-PPy composite after testing.

reproducibility. In addition, 50 CV scans were run in the same analyte and an average change of 2.15 μA (4.1% of the original) in oxidative peak responses was recorded for all electrodes. Regression values obtained from different techniques used in this study were compared (Fig. 8a) to obtain an average statistical confidence value 0.969306, which is quite high. The SEM result for Cu-PPy was obtained after the detection study of catechol, as shown in Fig. 8b. No significant change in surface morphology was observed.

4 Conclusion

Using a glassy carbon electrode (GCE) modified with a copper-polypyrrole (Cu-PPy) composite, we synthesized an enzyme-free, highly selective biosensor for catechol detection. As copper nanoparticles occupied the voids within or on the surface of polypyrrole, shifts in peaks were recorded, as evidenced by XRD, SEM, FTIR, and Raman spectroscopic analysis. GCE@Cu-PPy showed superior sensing qualities for the detection of CAT, including a low detection limit (1.52×10^{-7} μM), high linear range (0.02–2500 μM), excellent selectivity, and greater storage stability at a recovery rate of 93.68%. The GCE@Cu-PPy application was successfully implemented by detecting catechol in a real sample in the presence of its isomers and interfering species in high concentrations. Based on the statistical analysis of all the methods used in this study, the regression coefficient (R^2) was found to be 0.969306. A higher statistical confidence value (R^2) provides proof that the Cu-PPy composite can be used as a catechol biosensor.

Conflicts of interest

The authors declare that they have no known financial or intellectual conflicts of interest that could have affected this research.

Acknowledgements

References

1 R. Joober, *et al.*, Catechol-O-Methyltransferase Val-108/158-Met Gene Variants Associated With Performance on the Wisconsin Card Sorting Test, *Arch. Gen. Psychiatry*, 2002, **59**(7), 662–663.

2 D. Kaneko, K. Matsumoto, S. Kinugawa, S. Tateyama and T. Kaneko, Effects of adhesive characteristics of the catechol group on fiber-reinforced plastics, *Polym. J.*, 2011, **43**(11), 944–947, DOI: 10.1038/pj.2011.91.

3 V. A. Fitsanakis, V. Amarnath, J. T. Moore, K. S. Montine, J. Zhang and T. J. Montine, Catalysis of catechol oxidation by metal-dithiocarbamate complexes in pesticides, *Free Radicals Biol. Med.*, 2002, **33**(12), 1714–1723, DOI: 10.1016/S0891-5849(02)01169-3.

4 J. Moreno-Andrés, I. Vallés, P. García-Negueroles, L. Santos-Juanes and A. Arques, Enhancement of Iron-Based Photo-Driven Processes by the Presence of Catechol Moieties, *Catalysts*, 2021, **11**(3), 372, DOI: 10.3390/catal11030372.

5 Y. Liu, H. Zhou, J. Wang, S. Li, Z. Li and J. Zhang, Core-shell Fe3O4@catechol-formaldehyde trapped satellite-like silver nanoparticles toward catalytic reduction in cationic and anionic dyes, *Vacuum*, 2022, **202**, 111204, DOI: 10.1016/j.vacuum.2022.111204.

6 H. Huang, Y. Chen, Z. Chen, J. Chen, Y. Hu and J.-J. Zhu, Electrochemical sensor based on Ce-MOF/carbon nanotube composite for the simultaneous discrimination of hydroquinone and catechol, *J. Hazard. Mater.*, 2021, **416**, 125895, DOI: 10.1016/j.jhazmat.2021.125895.

7 N. Schweigert, J. L. Acero, U. von Gunten, S. Canonica, A. J. Zehnder and R. I. Eggen, DNA degradation by the mixture of copper and catechol is caused by DNA-copper-hydroperoxy complexes, probably DNA-Cu(I)OOH," (in eng), *Environ. Mol. Mutagen.*, 2000, **36**(1), 5–12, DOI: 10.1002/1098-2280(2000)36:1<5::aid-em2>3.0.co;2-4.

8 Q. Liu, *et al.*, Activated carbon prepared from catechol distillation residue for efficient adsorption of aromatic organic compounds from aqueous solution, *Chemosphere*, 2021, **269**, 128750, DOI: 10.1016/j.chemosphere.2020.128750.

9 X. Wei, *et al.*, Deciphering the Changes of Sludge Toxicity and the Succession of Dominant Bacteria During the Process of Catechol Degradation by Acclimated Sludge, *Waste Biomass Valorization*, 2022, **13**, 4285–4296, DOI: 10.1007/s12649-022-01774-1.

10 J. Chakraborty, C. Suzuki-Minakuchi, T. Tomita, K. Okada, H. Nojiri and I. Cann, A Novel Gene Cluster Is Involved in the Degradation of Lignin-Derived Monoaromatics in Thermus oshimai JL-2, *Appl. Environ. Microbiol.*, 2021, **87**(11), e01589, DOI: 10.1128/AEM.01589-20.

11 X. Wu, *et al.*, Lignin-First Monomers to Catechol: Rational Cleavage of C–O and C–C Bonds over Zeolites, *ChemSusChem*, 2022, **15**(7), e202102248, DOI: 10.1002/cssc.202102248.

12 H. Wang, L. Wang, S. Zhang, W. Zhang, J. Li and Y. Han, Mussel-inspired polymer materials derived from nonphytogenic and phytogenic catechol derivatives and their applications, *Polym. Int.*, 2021, **70**(9), 1209–1224, DOI: 10.1002/pi.6230.

13 Z. An, *et al.*, Unravelling the effects of complexation of transition metal ions on the hydroxylation of catechol over the whole pH region, *J. Environ. Sci.*, 2022, **115**, 392–402, DOI: 10.1016/j.jes.2021.08.011.

14 X. Wang, J. Xiao and W. Tang, Hydroquinone versus Pyrocatechol Pendants Twisted Conjugated Polymer

Cathodes for High-Performance and Robust Aqueous Zinc-Ion Batteries, *Adv. Funct. Mater.*, 2022, **32**(4), 2108225, DOI: **10.1002/adfm.202108225**.

15 Y. Xu, T. Huang, S. Wang, M. Meng and Y. Yan, SiO2-coated molecularly imprinted sensor based on Si quantum dots for selective detection of catechol in river water, *J. Environ. Chem. Eng.*, 2022, **10**(1), 106850, DOI: **10.1016/j.jece.2021.106850**.

16 H. Li, *et al.*, Detection of catecholamine metabolites in urine based on ultra-high-performance liquid chromatography–tandem mass spectrometry, *Biomed. Chromatogr.*, 2022, **36**(3), e5280, DOI: **10.1002/bmc.5280**.

17 T. Shapterhasmi, N. Palani, M. Velusamy, N. S. P. Bhuvanesh, K. Sundaravel and S. Easwaramoorthi, Iron(III) complexes of pyrrolidine and piperidine appended tridentate 3N donor ligands as models for catechol dioxygenase enzymes, *Inorg. Chim. Acta*, 2022, **537**, 120924, DOI: **10.1016/j.ica.2022.120924**.

18 R. Li, D. Zhang, X. Li and H. Qi, Sensitive and selective electrogenerated chemiluminescence aptasensing method for the determination of dopamine based on target-induced conformational displacement, *Bioelectrochemistry*, 2022, **146**, 108148, DOI: **10.1016/j.bioelechem.2022.108148**.

19 A. Kilic, R. Söylemez and V. Okumuş, Design, spectroscopic properties and effects of novel catechol spiroborates derived from Schiff bases in the antioxidant, antibacterial and DNA binding activity, *J. Organomet. Chem.*, 2022, **960**, 122228, DOI: **10.1016/j.jorganchem.2021.122228**.

20 J. Delgado-Avilez, G. A. Huerta-Miranda, R. Jaimes-López and M. Miranda-Hernández, Theoretical study of the chemical interactions between carbon fiber ultramicroelectrodes and the dihydroxybenzene isomers for electrochemical sensor understanding, *Electrochim. Acta*, 2022, **402**, 139576, DOI: **10.1016/j.electacta.2021.139576**.

21 D. Li, *et al.*, Tannic acid as an eco-friendly natural passivator for the inhibition of pyrite oxidation to prevent acid mine drainage at the source, *Appl. Surf. Sci.*, 2022, **591**, 153172, DOI: **10.1016/j.apsusc.2022.153172**.

22 A. Maziz, E. Özgür, C. Bergaud and L. Uzun, Progress in conducting polymers for biointerfacing and biorecognition applications, *Sensors and Actuators Reports*, 2021, **3**, 100035, DOI: **10.1016/j.snr.2021.100035**.

23 Q.-l. Zhang, Z.-m. Yang, B.-j. Ding, X.-z. Lan and Y.-j. Guo, Preparation of copper nanoparticles by chemical reduction method using potassium borohydride, *Trans. Nonferrous Met. Soc. China*, 2010, **20**, s240–s244, DOI: **10.1016/S1003-6326(10)60047-7**.

24 M. T. Ramesan, Synthesis, characterization, and conductivity studies of polypyrrole/copper sulfide nanocomposites, *J. Appl. Polym. Sci.*, 2013, **128**(3), 1540–1546, DOI: **10.1002/app.38304**.

25 B. Thirumalraj, S. Palanisamy, S.-M. Chen, K. Thangavelu, P. Periakaruppan and X.-H. Liu, A simple electrochemical platform for detection of nitrobenzene in water samples using an alumina polished glassy carbon electrode, *J.*

Colloid Interface Sci., 2016, **475**, 154–160, DOI: **10.1016/j.jcis.2016.04.042**.

26 N. Manousi, A. Kabir, K. G. Furton, G. A. Zachariadis and A. Anthemidis, Automated Solid Phase Extraction of Cd(II), Co(II), Cu(II) and Pb(II) Coupled with Flame Atomic Absorption Spectrometry Utilizing a New Sol-Gel Functionalized Silica Sorbent, *Separations*, 2021, **8**(7), DOI: **10.3390/separations8070100**.

27 D. L. A. de Faria, S. Venâncio Silva and M. T. de Oliveira, Raman microspectroscopy of some iron oxides and oxyhydroxides, *J. Raman Spectrosc.*, 1997, **28**(11), 873–878, DOI: **10.1002/(SICI)1097-4555(199711)28:11<873::AID-JRS177>3.0.CO;2-B**.

28 E. Daş and A. B. Yurtcan, Effect of carbon ratio in the polypyrrole/carbon composite catalyst support on PEM fuel cell performance, *Int. J. Hydrogen Energy*, 2016, **41**(30), 13171–13179, DOI: **10.1016/j.ijhydene.2016.05.167**.

29 Y. Yan, L. Wu, Q. Guo and S. Huang, A Novel Catechol Electrochemical Sensor Based on Cobalt Hexacyanoferrate/(CoHCF)/Au/SBA-15, *J. Anal. Bioanal. Tech.*, 2015, **6**, 1000290.

30 A. Salimi, L. Miranzadeh and R. Hallaj, Amperometric and voltammetric detection of hydrazine using glassy carbon electrodes modified with carbon nanotubes and catechol derivatives, *Talanta*, 2008, **75**(1), 147–156, DOI: **10.1016/j.talanta.2007.10.044**.

31 K. Chetankumar, B. E. K. Swamy and T. S. S. K. Naik, A reliable electrochemical sensor for detection of catechol and hydroquinone at MgO/GO modified carbon paste electrode, *J. Mater. Sci.: Mater. Electron.*, 2020, **31**(22), 19728–19740, DOI: **10.1007/s10854-020-04498-x**.

32 K. Castro, *et al.*, Galactodendritic Porphyrinic Conjugates as New Biomimetic Catalysts for Oxidation Reactions, *Inorg. Chem.*, 2015, **54**(9), 4382–4393, DOI: **10.1021/acs.inorgchem.5b00196**.

33 B. Liu, *et al.*, Electrochemical sensor based on covalent organic frameworks/MWCNT for simultaneous detection of catechol and hydroquinone, *Colloids Surf., A*, 2022, **639**, 128335, DOI: **10.1016/j.colsurfa.2022.128335**.

34 Z. Liu, D. Liao, J. Yu and X. Jiang, An electrochemical sensor based on oxygen-vacancy cobalt–aluminum layered double hydroxides and hydroxylated multiwalled carbon nanotubes for catechol and hydroquinone detection, *Microchem. J.*, 2022, **175**, 107216, DOI: **10.1016/j.microc.2022.107216**.

35 X. Yang, *et al.*, Electrochemical sensors for hydroquinone and catechol based on nano-flake graphite and activated carbon sensitive materials, *Synth. Met.*, 2022, **287**, 117079, DOI: **10.1016/j.synthmet.2022.117079**.

36 Z.-C. Fan, X.-Y. Wei, Z.-W. Tong, H.-R. Wang and Z.-M. Zong, In situ polymerization synthesis of polyaniline/strontium niobate nanocomposite for highly sensitive electrochemical detection of catechol, *J. Mater. Sci.*, 2022, **57**, 11523–11536, DOI: **10.1007/s10853-022-07319-0**.

37 X. Jiaojiao, W. Pengyun, Z. Bin and A. I. Onyinye, Enhancing electrochemical sensing for catechol by biomimetic oxidase covalently functionalized graphene oxide, *Bioprocess Biosyst. Eng.*, 2021, **44**(2), 343–353, DOI: **10.1007/s00449-020-02446-x**.

38 M. Arsalan, *et al.*, Enhanced Sensitive Electrochemical Sensor for Simultaneous Catechol and Hydroquinone Detection by Using Ultrasmall Ternary Pt-based Nanomaterial, *Electroanalysis*, 2021, **33**(6), 1528–1538, DOI: **10.1002/elan.202100026**.

39 W. Long, *et al.*, Preparation of nitrogen-doped hollow carbon spheres for sensitive catechol electrochemical sensing, *Fullerenes, Nanotubes, Carbon Nanostruct.*, 2018, **26**(12), 856–862, DOI: **10.1080/1536383X.2018.1512973**.

40 H. Noh, S. J. Lee, H. J. Jo, H. W. Choi, S. Hong and K. H. Kong, Histidine residues at the copper-binding site in human tyrosinase are essential for its catalytic activities, *J. Enzyme Inhib. Med. Chem.*, 2020, **35**(1), 726–732, DOI: **10.1080/14756366.2020.1740691**.

41 N. Aravindan, S. Preethi and M. V. Sangaranarayanan, Non-Enzymatic Selective Determination of Catechol Using Copper Microparticles Modified Polypyrrole Coated Glassy Carbon Electrodes, *J. Electrochem. Soc.*, 2017, **164**(6), B274, DOI: **10.1149/2.1601706jes**.